

STATE SPACE GEOMETRY OF A SPATIO-TEMPORALLY CHAOTIC KURAMOTO-SIVASHINSKY FLOW

PREDRAG CVITANOVIĆ* RUSLAN L. DAVIDCHACK† AND EVANGELOS SIMINOS*

Abstract. We show on the example of Kuramoto-Sivashinsky system that the geometry of a dynamical state space in presence of a continuous symmetry is organized by a rigid ‘cage’ built by heteroclinic connections between equilibria and relative periodic orbits, and demonstrate the preponderance of unstable relative periodic orbits and their likely role as the skeleton underpinning spatiotemporal turbulence in systems with continuous symmetries.

Rewrite,

Key words. periodic orbits, chaos, turbulence, Kuramoto-Sivashinsky equation

AMS subject classifications. 35B05, 35B10, 37L05, 37L20, 76F20, 65H10, 90C53

1. Introduction. Recent experimental and theoretical advances [11] support a dynamical vision of turbulence: For any finite spatial resolution, a turbulent flow follows approximately for a finite time a pattern belonging to a finite alphabet of admissible patterns. The long term dynamics is a walk through the space of these unstable patterns. The question is how to characterize and classify such patterns? Here we follow the seminal Hopf [13] paper, and visualize turbulence not as a sequence of spatial snapshots in turbulent evolution, but as a trajectory in an ∞ - d state space in which an instant in turbulent evolution is a unique point. In the dynamical systems approach, theory of turbulence for a given system, with given boundary conditions, is given by the (a) geometry of the state space and (b) the associated natural measure, that is, the likelihood that asymptotic dynamics visits a given state space region.

Here we pursue this program in context of the Kuramoto-Sivashinsky (KS) equation, one of the simplest physically interesting spatially extended nonlinear systems. Holmes, Lumley and Berkooz [12] offer a delightful discussion of why this system deserves study as a staging ground for studying turbulence in full-fledged Navier-Stokes boundary shear flows.

Dynamical state space representation of a PDE is ∞ -dimensional, but the KS flow is strongly contracting and its non-wandering set, and, within it, the set of invariant solutions investigated here, is embedded into a finite-dimensional inertial manifold [6] in a non-trivial, nonlinear way. ‘Geometry’ in the title of this paper refers to our attempt to systematically triangulate this set in terms of a dynamically invariant solutions (equilibria, periodic orbits, ...) and their unstable manifolds, in a PDE representation and DNS algorithm independent way. The goal is to describe a given ‘turbulent’ flow quantitatively, not model it qualitatively by a low-dimensional model. For the case investigated here, the state space representation dimension $d \sim 10^2$ is set by requiring that the exact invariant solutions that we compute are accurate to $\sim 10^{-5}$. The state space is high-dimensional, the asymptotic dynamics is confined to a low-dimensional subspace, so we are in the gray, ill-defined overlapping zone between ‘turbulence’ and ‘spatiotemporal chaos,’ the two terms that we shall use interchangeably in what follows.

In previous work, the state space geometry and the natural measure for this system have been studied [3, 19, 20] in terms of unstable periodic solutions restricted to the antisymmetric subspace of the KS dynamics.

*School of Physics, Georgia Institute of Technology, Atlanta, GA 30332-0430, USA

†Department of Mathematics, University of Leicester, University Road, Leicester LE1 7RH, UK

The focus in this paper is on the role continuous symmetries play in spatiotemporal dynamics. The notion of exact periodicity in time is replaced by the notion of relative spatiotemporal periodicity, and relative equilibria and relative periodic orbits here play the role the equilibria and periodic orbits played in the earlier studies.

Building upon the pioneering work of refs. [16, 10], we undertake here a study of the Kuramoto-Sivashinsky dynamics for a specific system size $L = 22$, sufficiently large to exhibit many of the features typical of ‘turbulent’ dynamics observed in large KS systems, but small enough to lend itself to a detailed exploration of the equilibria and relative equilibria, their stable/unstable manifolds, determination of a large number of relative periodic orbits, and a preliminary exploration of the relation between the observed spatiotemporal ‘turbulent’ patterns and the relative periodic orbits.

In presence of a continuous symmetry any solution belongs to a group manifold of equivalent solutions. The problem: If one is to generalize the periodic orbit theory to this setting, one needs to understand what is meant by solutions being nearby (shadowing) when each solution belongs to a manifold of equivalent solutions. We resolve here this puzzle by demonstrating that if one picks any particular solution, the universe of all other solutions is rigidly fixed through a web of heteroclinic connections between them. This insight garnered from study of a 1-dimensional Kuramoto-Sivashinsky PDE is more remarkable still when applied to the plane Couette flow [9], with 3-d velocity fields and two translational symmetries.

The main results presented here are: (a) Dynamics visualized through physical, symmetry invariant observables, such as ‘energy,’ dissipation rate, *etc.*, and through projections onto a dynamically invariant, PDE-discretization independent state space coordinate frames, sect. 3. (b) Existence of a rigid ‘cage’ built by heteroclinic connections between equilibria and periodic orbits, sect. 4. (c) Preponderance of unstable relative periodic orbits and their likely role as the skeleton underpinning spatiotemporal turbulence in systems with continuous symmetries, sect. 6.

2. Kuramoto-Sivashinsky equation. The Kuramoto-Sivashinsky [henceforth KS] system [18, 24], which arises in the description of stability of flame fronts, reaction-diffusion systems and many other physical settings [16], is one of the simplest nonlinear PDEs that exhibit spatiotemporally chaotic behavior. In the formulation adopted here, the time evolution of the ‘flame front velocity’ $u = u(x, t)$ on a periodic domain $u(x, t) = u(x + L, t)$ is given by

$$u_t + \frac{1}{2}(u^2)_x + u_{xx} + u_{xxxx} = 0, \quad x \in [-L/2, L/2]. \quad (2.1)$$

Here $t \geq 0$ is the time, and x is the spatial coordinate. The subscripts x and t denote partial derivatives with respect to x and t . In what follows we shall state results of all calculations either in units of the ‘dimensionless system size’ \tilde{L} , or the system size $L = 2\pi\tilde{L}$. All numerical results presented in this paper are for the system size $\tilde{L} = 22/2\pi = 3.5014\cdots$. Spatial periodicity $u(x, t) = u(x + L, t)$ makes it convenient to work in the Fourier space,

$$u(x, t) = \sum_{k=-\infty}^{+\infty} a_k(t) e^{ikx/\tilde{L}}, \quad (2.2)$$

with the 1-dimensional PDE (2.1) replaced by an infinite set of ODEs for the complex Fourier coefficients $a_k(t)$:

$$\dot{a}_k = v_k(a) = ((k/\tilde{L})^2 - (k/\tilde{L})^4) a_k - i \frac{k}{2\tilde{L}} \sum_{m=-\infty}^{+\infty} a_m a_{k-m}. \quad (2.3)$$

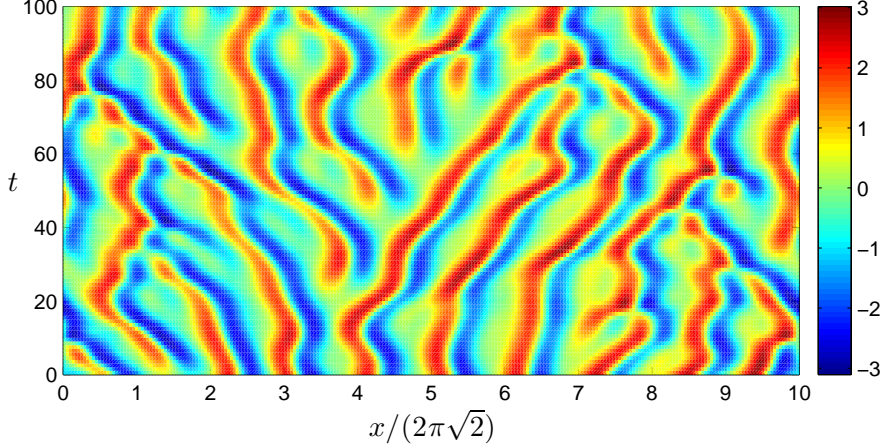


FIG. 2.1. A typical ‘turbulent’ solution of the Kuramoto-Sivashinsky equation, system size $L = 20\pi\sqrt{2} \approx 88.86$. The x coordinate is scaled with the most unstable wavelength $2\pi\sqrt{2}$, which is approximately also the mean wavelength of the turbulent flow. The color bar indicates the color scheme for $u(x, t)$. This color scheme is used in other figures of this type throughout this work.

Since $u(x, t)$ is real, $a_k = a_{-k}^*$, and we can replace the sum by a $k > 0$ sum.

¹ Due to the hyperviscous damping u_{xxxx} , long time solutions of Kuramoto-Sivashinsky equation are smooth, a_k drop off fast² with k , and truncations of (2.3) to $16 \leq d \leq 128$ terms yield accurate solutions for system sizes considered here. Robustness of the long-time dynamics of KS as a function of the number of Fourier modes kept in truncations of (2.3) is, however, a subtle issue. Adding an extra mode to a truncation of the system introduces a small perturbation in the space of dynamical systems. However, due to the lack of structural stability both as a function of truncation d , and the system size \tilde{L} , a small variation in a system parameter can (and often will) throw the dynamics into a different asymptotic state. For example, asymptotic attractor which appears to be chaotic in a d -dimensional state space truncation can collapse into an attractive period- n cycle for $(d+1)$ -dimensions.

2.1. Symmetries of Kuramoto-Sivashinsky equation. The KS equation is Galilean invariant: if $u(x, t)$ is a solution, then $u(x - \textcolor{red}{ct}, t) - \textcolor{red}{c}$, with c an arbitrary constant speed, is also a solution. Without loss of generality, in our calculations we shall set the mean velocity of the front to zero,

$$\int dx u = 0. \quad (2.4)$$

As $a_0 = 0$ in (2.3), a_0 is a conserved quantity, in our calculations fixed to $a_0 = 0$ by the condition (2.4). G , the group of actions $g \in G$ on a state space (reflections, translations, etc.) is a symmetry of the flow $\dot{u} = F(u)$ if $g\dot{u} = F(gu)$. The KS equation

$$\dot{u} = F(u) = -uu_x - u_{xx} - u_{xxxx} \quad (2.5)$$

¹PC: find better place for this text?

²PC: how fast?

is time translationally invariant, and space translationally invariant on a periodic domain under the 1-parameter group of $O(2) : \{\tau_{\ell/L}, R\}$. If $u(x, t)$ is a solution, then $\tau_{\ell/L} u(x) = u(x + \ell, t)$ is an equivalent solution for any shift $-L/2 < \ell \leq L/2$, as is the reflection ('parity' or 'inversion')

$$R u(x) = -u(-x). \quad (2.6)$$

The translation operator action on the Fourier coefficients

$$(\tau_{\ell/L} a)_k = e^{ik\ell/\tilde{L}} a_k \quad (\text{no summation on } k). \quad (2.7)$$

amounts to the k -th mode complex plane rotation by an angle $-k\ell/\tilde{L}$, and the reflections acts on them by complex conjugation,

$$R a_k = -a_k^*. \quad (2.8)$$

Reflection generates the dihedral subgroup $D_1 = \{1, R\}$ of $O(2)$. Let \mathbb{U} be the space of real-valued velocity fields periodic and square integrable on the interval $\Omega = [-L/2, L/2]$,

$$\mathbb{U} = \{u \in L^2(\Omega) \mid u(x) = u(x + L)\}. \quad (2.9)$$

A continuous symmetry maps each state $u \in \mathbb{U}$ to a manifold of functions with identical dynamic behavior. Relation $R^2 = 1$ induces linear decomposition $u(x) = u^+(x) + u^-(x)$, $u^\pm(x) = P^\pm u(x) \in \mathbb{U}^\pm$, into irreducible subspaces $\mathbb{U} = \mathbb{U}^+ \oplus \mathbb{U}^-$, where

$$P^+ = (\mathbf{1} + R)/2, \quad P^- = (\mathbf{1} - R)/2 \quad (2.10)$$

are the antisymmetric/symmetric projection operators. Applying P^+ , P^- on the KS equation (2.5) we have [16]

$$\begin{aligned} u_t^+ &= -(u^+ u_x^+ + u^- u_x^-) - u_{xx}^+ - u_{xxxx}^+ \\ u_t^- &= -(u^+ u_x^- + u^- u_x^+) - u_{xx}^- - u_{xxxx}^-. \end{aligned} \quad (2.11)$$

If $u^- = 0$, KS flow is confined to the antisymmetric \mathbb{U}^+ subspace,

$$u_t^+ = -u^+ u_x^+ - u_{xx}^+ - u_{xxxx}^+, \quad (2.12)$$

but otherwise the nonlinear terms in (2.11) mix the two subspaces.³

Together with any rational shift $\tau_{1/m} u(x) = u(x + L/m)$ reflection generates a discrete dihedral D_m subgroup of $O(2)$, also a symmetry of KS. The only non-zero Fourier components of a solution invariant under D_m are $a_{jm} \neq 0$, $j = 1, 2, \dots$. D_m reduces the dimensionality of state space and aids computation of equilibria and periodic orbits within it. For example, the 1/2-cell translations⁴

$$\tau_{1/2} u(x) = u(x + L/2), \quad (2.13)$$

³PC: still to be incorporated, most likely in the next paper: wrote down (2.11) in order to (a) to clarify embedding of \mathbb{U}^+ into \mathbb{U} (b) to explain the desymmetrization of evolution defined on $\Omega^+ = [0, L/2]$ fundamental domain, with evolution at instant of crossing $x = 0$ given by reflection R . Re integrators: make sure R applied after all points used by integrator are in \mathbb{U}^-

⁴ES: moved all references to 1/2-cell translation to one place.

and reflections generate $O(2)$ subgroup $D_2 = \{1, R, \tau, \tau R\}$, which reduces the state space into four irreducible subspaces (for brevity, here $\tau = \tau_{1/2}$):⁵

$$\begin{array}{lll} & \tau & R \quad \tau R \\ P^{(1)} & = \frac{1}{4}(1 + \tau + R + \tau R) & S \quad A \quad A \\ P^{(2)} & = \frac{1}{4}(1 + \tau - R - \tau R) & S \quad S \quad S \\ P^{(3)} & = \frac{1}{4}(1 - \tau + R - \tau R) & A \quad A \quad S \\ P^{(4)} & = \frac{1}{4}(1 - \tau - R + \tau R) & A \quad S \quad A. \end{array} \quad (2.14)$$

$P^{(j)}$ is the projection operator onto $u^{(j)}$ irreducible subspace, and the last 3 columns refer to the symmetry of $u^{(j)}$ functions under reflection and 1/2-cell shift. By the same argument that identified (2.12) as the invariant subspace of KS, here the KS flow stays within the $\mathbb{U}^S = \mathbb{U}^{(1)} + \mathbb{U}^{(2)}$ irreducible D_1 subspace of \mathbb{U} profiles symmetric under 1/2-cell shifts.

⁶ While in general the bilinear term $(u^2)_x$ mixes the irreducible subspaces of D_n , for D_2 there are four subspaces invariant under the flow [16]:

{0}: the $u(x) = 0$ equilibrium

$\mathbb{U}^+ = \mathbb{U}^{(1)} + \mathbb{U}^{(3)}$: the reflection D_1 irreducible space of antisymmetric $u(x)$

$\mathbb{U}^S = \mathbb{U}^{(1)} + \mathbb{U}^{(2)}$: the shift D_1 irreducible space of $L/2$ shift symmetric $u(x)$

$\mathbb{U}^{(1)}$: the D_2 irreducible space of $u(x)$ invariant under $x \mapsto L/2 - x$, $u \mapsto -u$

as long as all other components of $u(x)$ are set to zero (see for example (2.12)). With the continuous translational symmetry eliminated within each subspace, there are no relative equilibria and relative periodic orbits, and one can focus on the equilibria and periodic orbits only, as was done for \mathbb{U}^+ in refs. [3, 19, 20]. In the Fourier representation, the $u \in \mathbb{U}^+$ antisymmetry amounts to having purely imaginary coefficients, since $a_{-k} = a_k^* = -a_k$. The 1/2 cell-size shift $\tau_{1/2}$ generated 2-element discrete subgroup $\{1, \tau_{1/2}\}$ is of particular interest because in the \mathbb{U}^+ subspace the translational invariance of the full system reduces to invariance under discrete translation (2.13) by half a spatial period $L/2$.

Each of the above dynamically invariant subspaces is unstable under small perturbations, and generic solutions of Kuramoto-Sivashinsky equation belong to the full space. Nevertheless, since all equilibria of the KS flow studied in this paper lie in the \mathbb{U}^+ subspace (see sect. 4), \mathbb{U}^+ plays important role for the global geometry of the flow. However, linearized stability of these equilibria has eigenvectors both in and outside of \mathbb{U}^+ , and needs to be computed in the full state space.

2.2. Equilibria and relative equilibria. Equilibria (or the steady solutions) are the fixed profile time-invariant solutions,

$$u(x, t) = u_q(x). \quad (2.15)$$

Due to the translational symmetry, the KS system also allows for relative equilibria (traveling waves, rotating waves), characterized by a fixed profile $u_q(x)$ moving with

⁵PC: dangerous edit, changed $S \rightarrow A$ for reflections, please cross-check

⁶PC: abandoned the ref. [16] notation, I might be wrong, please recheck. Replace $\mathbf{L} \rightarrow P^{(1)}$ downstream

constant speed c , that is

$$u(x, t) = u_q(x - ct). \quad (2.16)$$

Here suffix q labels a particular invariant solution. Because of the reflection symmetry (2.6), the relative equilibria come in counter-traveling pairs $u_q(x - ct)$, $-u_q(-x + ct)$.

The relative equilibrium condition for the Kuramoto-Sivashinsky PDE (2.1) is the ODE

$$\frac{1}{2}(u^2)_x + u_{xx} + u_{xxxx} = c u_x \quad (2.17)$$

which can be analyzed as a dynamical system in its own right.⁷ Integrating once we get⁸

$$\frac{1}{2}u^2 - cu + u_x + u_{xxx} = E. \quad (2.18)$$

The integration constant E can be interpreted as ‘energy’, see sect. 3. Written as a 3-dimensional dynamical system with spatial coordinate x playing the role of ‘time’, this is a volume preserving flow

$$v = u_x, \quad w = v_x, \quad w_x = E - \frac{1}{2}u^2 + cu - v, \quad (2.19)$$

⁹ with the ‘time’ reversal symmetry,

$$x \rightarrow -x, \quad u \rightarrow -u, \quad v \rightarrow v, \quad w \rightarrow -w. \quad c \rightarrow -c$$

¹⁰ ¹¹ Rewriting (2.19) as¹²

$$\begin{aligned} E - \frac{1}{2}(u - c)^2 + c^2 &= E + c^2 \\ (u + w)_x = \underbrace{\frac{1}{2}(u - c)^2 - E}_{(u + w)_x} &= \frac{1}{2}(u - c - \sqrt{2E})(u - c + \sqrt{2E}) \end{aligned} \quad (2.20)$$

we see that for $E < 0$,¹³ $u + w$ increases without bound with $x \rightarrow \infty$, and every solution escapes to infinity. If $E = 0$, the origin $(0, 0, 0)$ is the only bounded solution, a marginally stable center with eigenvalues $(0, i, -i)$.

For $E > 0$ there is rich E -dependent dynamics, with fractal sets of bounded solutions investigated in depth by Michelson [22]. For $\tilde{L} < 1$ the only equilibrium of the system is the globally attracting constant solution $u(x, t) = 0$, denoted E_0 from now on. With increasing system size L system undergoes a series of bifurcations. The resulting equilibria and relative equilibria (but not periodic orbits and relative periodic orbits) are described in the classical papers of Kevrekidis, Nicolaenko and Scovel [16], and Greene and Kim [10]. The relevant bifurcations up to the system size investigated here are summarized in Figure 2.2: at $\tilde{L} = 22/2\pi = 3.5014\cdots$, the equilibria are the constant solution E_0 , the GLMRT [23, 10] equilibrium E_1 , the 2- and 3-cell states E_2 and E_3 , the pair of relative equilibria $TW_{\pm 1}$, and the $TW_{\pm 2}$ relative equilibria.

⁷PC: PC: please recheck E vs c

⁸PC: relative equilibria = equilibria shifted by c ?

⁹ES: Changed signs here, seemed simpler this way. PC: I remember having a reason, so something down the line came out with consistent signs. Perhaps (2.20)?

¹⁰ES: The term cu breaks the symmetry. We may overcome this by changing sign of c as well, but it is a parameter, not a variable.

¹¹PC: might move space average def (3.1) to here, note that $\langle u \rangle = \langle v \rangle = \langle w \rangle = 0$

¹²ES: With the corrected form of (2.18) we cannot write this

¹³ES: Isn't $E > 0$ by definition? PC: Here E is an integration constant - do not see how we can argue $E \geq 0$ at this point.

eq (3.6)

Drop.

This equation
can be
interpreted
as a

3-dim
dynamical
system
with x
playing
the role
of time.

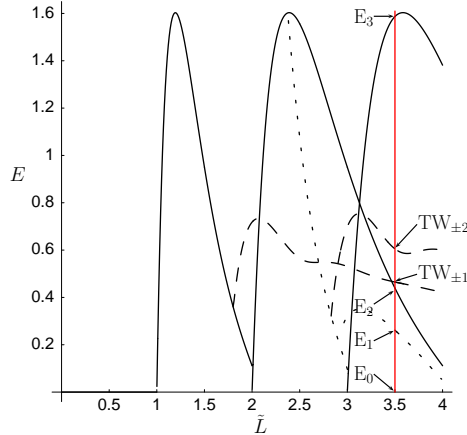


FIG. 2.2. The energy (3.6) of the equilibria and relative equilibria that exist up to $L = 22$, $\tilde{L} = 3.5014\cdots$, plotted as a function of the system size $\tilde{L} = L/2\pi$ (additional equilibria, not present at $L = 22$ are given in ref. [10]). Solid curves denote n -cell solutions E_2 and E_3 , dotted curves the GLMRT equilibrium E_1 , and dashed curves the relative equilibria $TW_{\pm 1}$ and $TW_{\pm 2}$. The parameter α of refs. [16, 10] is related to the system size by $\tilde{L} = \sqrt{\alpha/4}$.

14

In the Fourier representation the relative equilibria time dependence is

$$a_k(t)e^{-itck/\tilde{L}} = a_k(0). \quad (2.21)$$

Differentiating with respect to time, we obtain the Fourier space version of the relative equilibrium condition

$$v_k(a) - i\frac{kc}{\tilde{L}}a_k = 0, \quad (2.22)$$

we solve

which needs to be solved for (time independent) a_k and c . For a periodic boundary cell of size L the only equilibria are solutions of (2.19) of spatial periodicity L . Periods of spatially periodic equilibria are multiples of L . Every time the system size crosses $\tilde{L} = n$, n -cell states are generated through pitchfork bifurcations off $u = 0$ equilibrium. Due to the translational invariance of Kuramoto-Sivashinsky equation, they form invariant circles in the full state space. In the discrete symmetry subspace considered here, they correspond to two points, one $L/2$ shift of the other.

For any fixed period L the number of spatially periodic solutions is finite up to a spatial translation. For a sufficiently small L the number of equilibria is small and concentrated on the low wave-number end of the Fourier spectrum.

In a periodic box of size L both equilibria and relative equilibria are periodic solutions embedded in 3-d space (2.19), conveniently represented as loops in (u, u_x, u_{xx}) space¹⁵, see Figure 5.1 (d). In this representation the continuous translation symmetry is automatic — a rotation in the $[0, L]$ periodic domain only moves the points along the loop. For an equilibrium the points are stationary in time; for relative equilibrium

¹⁴ES: Removed text about equilibria of equilibria.

¹⁵ES: dropped whose topology is controlled by the ‘equilibria of equilibria’ stable-unstable manifold structure of (??)

u^+

(u, u_x, u_{xx})

they move in time, but in either case, the loop remains invariant. So we do not have the problem that we encounter in the Fourier representation, where from the frame of one of the equilibria the rest trace out circles under the action of continuous symmetry translations.

2.3. Stability of equilibria. If $u_q(x)$ is an equilibrium solution of Kuramoto-Sivashinsky equation, the stability matrix $A = A(a_q)$ is constant in time, and the fundamental matrix of the equilibrium solution is

$$J^t(a_q) = e^{At}, \quad A_{ij} = A_{ij}(a_q). \quad (2.23)$$

Calculation of the stability matrix requires a bit of care: a_k cannot be varied independently of a_{-k} , as the reality of $u(x, t)$ implies that $a_k = a_{-k}^*$. We impose the reality constraint by splitting (2.3) in real and imaginary parts, $a_k = b_k + i c_k$. Stability matrix is then:

$$\begin{aligned} \frac{\partial \dot{c}_k}{\partial c_j} &= \frac{k^2}{\tilde{L}^2} \left(1 - \frac{k^2}{\tilde{L}^2}\right) \delta_{kj} - \frac{k}{\tilde{L}} (c_{k+j} - c_{k-j}) \\ \frac{\partial \dot{c}_k}{\partial b_j} &= -\frac{k}{\tilde{L}} (b_{k+j} + b_{k-j}) \\ \frac{\partial \dot{b}_k}{\partial b_j} &= \frac{k^2}{\tilde{L}^2} \left(1 - \frac{k^2}{\tilde{L}^2}\right) \delta_{kj} + \frac{k}{\tilde{L}} (c_{k+j} + c_{k-j}) \\ \frac{\partial \dot{b}_k}{\partial c_j} &= -\frac{k}{\tilde{L}} (b_{k+j} - b_{k-j}), \quad k, j > 0. \end{aligned} \quad (2.24)$$

For the Kuramoto-Sivashinsky equation the constant solution $u(x, t) = 0$ with zero energy E is an equilibrium point of (2.1) which we shall henceforth refer to as E_0 . For this ‘laminar’ equilibrium the stability matrix is diagonal, and so is the fundamental matrix $J_{kj}^t(0) = \delta_{kj} e^{(k/\tilde{L})^2(1-(k/\tilde{L})^2)t}$.

From (2.3) we see that the origin $u(x, t) = 0$ has Fourier modes as the linear stability eigenvectors. The $|k| < \tilde{L}$ long wavelength perturbations of the flat-front equilibrium are linearly unstable, while all $|k| > \tilde{L}$ short wavelength perturbations are strongly contractive. The high k eigenvalues, corresponding to rapid variations of the flame front, decay so fast that the corresponding eigendirections are physically irrelevant. The most unstable mode, nearest to $|k| = \tilde{L}/\sqrt{2}$, sets the scale of the mean wavelength $\sqrt{2}$ of the KS ‘turbulent’ dynamics, see Figure 2.1.

2.4. Relative periodic orbits, symmetries and periodic orbits. The KS equation (2.1) is time translationally invariant, and space translationally invariant under the 1-d Lie group of $O(2)$ rotations: if $u(x, t)$ is a solution, then $u(x + \ell, t)$ and $-u(-x + \ell, t)$ are equivalent solutions for any $-L/2 < \ell \leq L/2$. As a result, KS can have relative periodic orbit solutions with period T and a nonzero shift ℓ , without or with reflection,

$$u(x + \ell, T) = u(x, 0), \quad \text{or} \quad -u(-x + \ell, T) = u(x, 0), \quad (2.25)$$

that is, a profile $u(x, 0)$ that occurs again after time T , but shifted by ℓ , and possibly reflected by R . Relative periodic orbits are periodic in $c = \ell/T$ co-rotating frame, but in the stationary frame their trajectories are quasiperiodic. Due to the reflection symmetry (2.6) of KS equation, every relative periodic orbit $u(x, t)$ with shift ℓ has a symmetric partner $-u(-x, t)$ with shift $-\ell$.

Move
to
Appendix

Evaluation
of
The stability
of r_{po}, p_o ,
equa is
discussed
in
Appendix

Our search for relative periodic orbits in KS system were inspired by Vanessa López [21] investigation of relative periodic orbits of the Complex Ginzburg-Landau equation. However, there is a vast literature on relative periodic orbits since their first appearance, in Poincaré study of the 3-body problem [2, 25] where the Lagrange points are the relative equilibria. They arise in dynamics of systems with continuous symmetries, such as motions of rigid bodies, gravitational N -body problems, molecules and nonlinear waves. Very recently Viswanath [26] has found both relative equilibria and relative periodic orbits in the plane Couette problem.

As ℓ is continuous in the interval $[-L/2, L/2]$, the likelihood of a $\ell = 0$ shift is zero, unless an exact periodicity is enforced by a discrete symmetry, such as the dihedral symmetries discussed above. If the shift ℓ of a relative periodic orbit with period T is such that ℓ/L is a rational number, then the orbit is periodic with period nT . Due to the KS equation invariance under reflection (2.6), two types of periodic orbits are possible:

(a) The periodic orbit lies within the \mathbb{U}^\dagger antisymmetric subspace $-u(-x, 0) = u(x, 0)$ and $u(x, T) = u(x, 0)$.

(b) The relative periodic orbit in (2.25) is of reflection type $R\tau_{\ell/L}u(x, T) = u(x, 0)$. In the next period T such orbit reverses its drift, $R\tau_{\ell/L}u(-x - \ell, 2T) = u(x, 0)$, and any shift acquired during time 0 to T is compensated by the opposite shift during evolution from T to $2T$. Periodic orbits built from repetitions of such shorter segments are encountered in dynamical systems with discrete symmetries [5, 4].¹⁶

3. Energy transfer rates. In physical settings where the observation times are much longer than the dynamical ‘turnover’ and Lyapunov times (statistical mechanics, quantum physics, turbulence) periodic orbit theory [4] provides highly accurate predictions of measurable long-time averages such as the turbulent drag [9]. Physical predictions have to be independent of a particular choice of ODE representation of the PDE under consideration and, most importantly, invariant under all symmetries of the dynamics. In this section we discuss a set of such physical observables for the 1D KS invariant under reflections and translations. They offer a representation of dynamics in which the symmetries are explicitly quotiented out. We illustrate this in sect. 6.3 by projecting a set of explicit solutions on these coordinates.

The space average of a function $a = a(x, t)$ on the interval L ,

$$\langle a \rangle = \frac{1}{L} \oint dx a(x, t), \quad (3.1)$$

is in general time dependent. Its mean value is given by the time average

$$\bar{a} = \lim_{t \rightarrow \infty} \frac{1}{t} \int_0^t d\tau \langle a \rangle = \lim_{t \rightarrow \infty} \frac{1}{t} \int_0^t \frac{1}{L} \oint d\tau dx a(x, \tau). \quad (3.2)$$

The mean value of $a = a(u_q) \equiv a_q$ evaluated on q equilibrium or relative equilibrium $u(x, t) = u_q(x - ct)$ is

$$\bar{a}_q = \langle a \rangle_q = a_q. \quad (3.3)$$

Evaluation of the infinite time average (3.2) on a function of a periodic orbit or relative periodic orbit $u_p(x, t) = u_p(x, t + T_p)$ requires only a single T_p traversal,

$$\bar{a}_p = \frac{1}{T_p} \int_0^{T_p} d\tau \langle a \rangle. \quad (3.4)$$

¹⁶PC: are there (c) periodic orbits which have D_m symmetries?

Equation (2.1) can be written as

$$u_t = -V_x, \quad V(x, t) = \frac{1}{2}u^2 + u_x + u_{xxx}. \quad (3.5)$$

~~u is related to the ‘flame-front height’ $h(x, t)$ by $u = h_x$, so E , defined in (2.18), can be interpreted as the mean energy density.~~ So, even though KS is a phenomenological small-amplitude equation, the time-dependent quantity

$$E = \frac{1}{L} \oint dx V(x, t) = \frac{1}{L} \oint dx \frac{u^2}{2} \quad (3.6)$$

has a physical interpretation [10] as the average ‘energy’ density of the flame front. This analogy to ~~the corresponding definition of~~ the mean kinetic energy density for the Navier-Stokes motivates what follows.

The energy (3.6) is intrinsic to the flow, independent of the particular ODE basis set chosen to represent the PDE. However, as the Fourier amplitudes are eigenvectors of the translation operator, in the Fourier space the energy is a diagonalized quadratic norm,

$$E = \sum_{k=-\infty}^{\infty} E_k, \quad E_k = \frac{1}{2}|a_k|^2, \quad (3.7)$$

and explicitly invariant term by term under translations (2.7).

Take time derivative of the energy density (3.6), substitute (2.1) and integrate by parts. Total derivatives vanish by the spatial periodicity on the L domain:

$$\begin{aligned} \dot{E} &= \langle u_t u \rangle = -\langle (u^2/2 + u u_x + u u_{xxx})_x u \rangle \\ &= \langle u_x u^2/2 + u_x^2 + u_x u_{xxx} \rangle. \end{aligned} \quad (3.8)$$

The first term in (3.8) vanishes by integration by parts, $3\langle u_x u^2 \rangle = \langle (u^3)_x \rangle = 0$, and integrating the third term by parts yet again one gets [10] that the energy variation

$$\dot{E} = P - D, \quad P = \langle u_x^2 \rangle, \quad D = \langle u_{xx}^2 \rangle \quad (3.9)$$

balances the power P pumped in by anti-diffusion u_{xx} against the energy dissipation rate D by hyper-viscosity u_{xxxx} in the KS equation (2.1).

The time averaged energy density \bar{E} computed on a typical orbit goes to a constant, so the expectation values (3.10) of drive and dissipation exactly balance each other:

$$\bar{E} = \lim_{t \rightarrow \infty} \frac{1}{t} \int_0^t d\tau \dot{E} = \bar{P} - \bar{D} = 0. \quad (3.10)$$

In particular, the equilibria and relative equilibria fall onto the diagonal in Figure 6.5, and so do time averages computed on periodic orbits and relative periodic orbits:

$$\bar{E}_p = \frac{1}{T_p} \int_0^{T_p} d\tau E(\tau), \quad \bar{P}_p = \frac{1}{T_p} \int_0^{T_p} d\tau P(\tau) = \bar{D}_p. \quad (3.11)$$

In the Fourier basis (3.7) the conservation of energy on average takes form

$$0 = \sum_{k=-\infty}^{\infty} ((k/\tilde{L})^2 - (k/\tilde{L})^4) \bar{E}_k, \quad E_k(t) = \frac{1}{2}|a_k(t)|^2. \quad (3.12)$$

The large k convergence of this series is insensitive to the system size L ; \bar{E}_k have to decrease much faster than $(k/\tilde{L})^{-4}$. ¹⁷ Deviation of E_k from this bound for small k

¹⁷PC: determine the decay rate, presumably exponential in k

If u is
flame-front
velocity,
then E

determines the active modes. This may be useful to bound the number of equilibria, with the upper bound given by zeros of a small number of long wavelength modes. For equilibria the L -independent bound on E is given by Michaelson [22]. The best current bound [8, 1] on the long-time limit of E as a function of the system size L scales as $E \propto L^{3/2}$.

Spatial representations of PDEs (such as the 3D snapshots of velocity and vorticity fields in Navier-Stokes) offer little insight into detailed dynamics of low- Re flows. Much more illuminating are the state space representations.¹⁸

4. Geometry of state space with $L = 22$. We now turn to exploring Hopf's vision numerically, on a specific Kuramoto-Sivashinsky system. An instructive example is offered by the dynamics for the $L = 22$ system that we specialize to for the rest of this paper. The size of this small system is ~ 2.5 mean wavelengths ($\tilde{L}/\sqrt{2} = 2.4758$),¹⁹ and the competition between wavenumbers 2 and 3 states leads to the empirically observed 'sustained turbulence.' Asymptotic attractor structure of small systems like the one studied here is very sensitive to system parameter variations, and, as is true of any realistic unsteady flow, there is no rigorous way of establishing that this 'turbulence' is sustained for all time, rather than being merely a very long transient on a way to an attracting periodic state. For large system size, as the one shown in Figure 2.1, it is hard to imagine a scenario under which attractive periodic states (as shown in ref. [7] they do exist) would have significantly large immediate basins of attraction. Regardless of the (non)existence of a $t \rightarrow \infty$ chaotic attractor, study of the invariant unstable solutions and the associated Smale horseshoe structures in system's state space offers valuable insights into the observed unstable 'coherent structures.'

Because of the strong k^4 contraction, for a small system size one expects that the long-time dynamics is confined to low-dimensional center manifold. Indeed, numerically the leading Lyapunov exponents of the $L = 22$ chaotic attractor are $(\lambda_i) = (0.048, 0, 0, -0.003, -0.189, -0.256, -0.290, \dots)$, so the chaotic dynamics mostly takes place close to a 4-dimensional manifold, with strong contraction in other dimensions. The two zero exponents are due to the time and space translational symmetries of the Kuramoto-Sivashinsky equation, and it was shown in refs. [3, 20] that within particular curvilinear coordinate frames, the dynamics on the attractor can sometimes be reduced to local 1- or 2-dimensional maps. Hence a relatively small number of Fourier modes truncations, of order of $d \sim 10^2$ for the system studied here, suffices to obtain numerically accurate (within 10^{-5}) invariant solutions.²⁰

We start ~~next investigate the properties of~~ relative periodic orbits for KS in a periodic cell of size $L = 22$.²¹

5. Equilibria and relative equilibria In addition to the trivial equilibrium $u = 0$ (denoted E_0), we find ~~for $L = 22$~~ three equilibria with dominant wavenumber k (denoted E_k) for $k = 1, 2, 3$. All equilibria, shown in Fig. 5.1, are symmetric with respect to the reflection symmetry (2.6). In addition, E_2 and E_3 are symmetric with respect to translation (2.13), by $L/2$ and $L/3$, respectively. E_2 and E_3 essentially lie, respectively, in the 2nd and 3rd Fourier component complex plane, with small

¹⁸PC: expand this into a visualization subsection: how we use d -dimensional vectors (stability eigenvectors, etc) to project from d -dimensions to 2 or 3 dimensions. Not Fourier modes as coordinates!

¹⁹PC: define this $\sqrt{2}$ in the theory section, refer to it here

²⁰PC: dropped "See Figure 6 in ref. [3]."

²¹PC: we have not proven "all" part

↓PRIVATE
↑PRIVATE } drop

↓PRIVATE } drop
↑PRIVATE

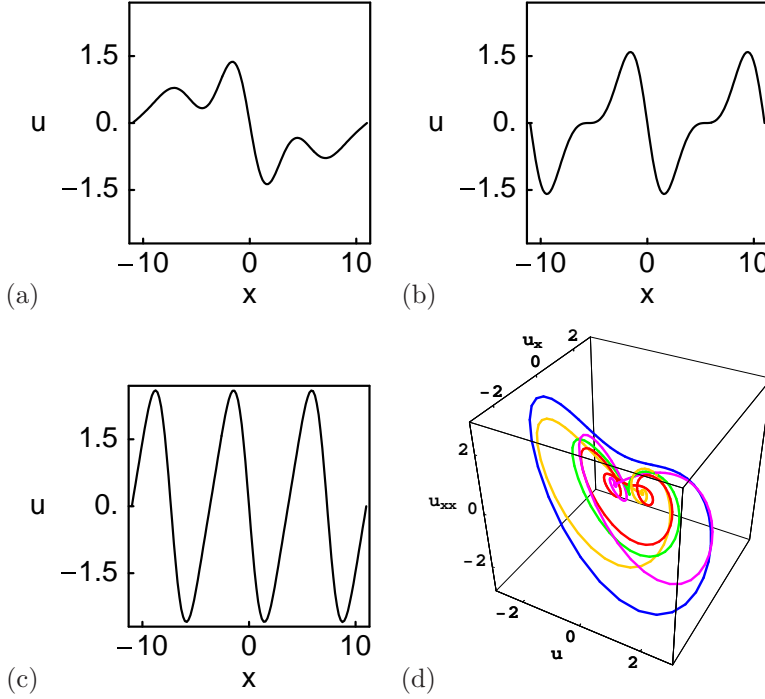


FIG. 5.1. (a) E_1 , (b) E_2 , and (c) E_3 equilibria. The E_0 equilibrium is the $u(x) = 0$ solution. (d) (u, u_x, u_{xx}) representation of (red) E_1 , (green) E_2 , (blue) E_3 equilibria, (purple) TW_{+1} , and (orange) TW_{-1} relative equilibria. $L = 22$ system size.

deformations from $k = 2j$, $k = 3j$ harmonics.²²

The stability of the equilibria is characterized by the eigenvalues λ_j of the stability matrix. The leading 10 eigenvalues for each equilibrium are listed in Table 5. We compute (available upon request) the corresponding eigenvectors as well. As an equilibrium with $\text{Re}\lambda_j > 0$ is unstable in the direction of the corresponding eigenvector $e^{(j)}$, the eigenvectors provide flow-intrinsic (PDE discretization independent) coordinates which we use for visualization of unstable manifolds and homo- / hetero-clinic connections between equilibria.

The eigenvalues of E_0 are determined by the linear part of the KS equation (2.24): $\lambda_k = (k/\tilde{L})^2 - (k/\tilde{L})^4$. For $L = 22$, there are three pairs of unstable eigenvalues, corresponding, in decreasing order, to three unstable modes $k = 2, 3$, and 1 . For each mode, the corresponding eigenvectors lie in the plane spanned by $\text{Re } a_k$ and $\text{Im } a_k$. Table 5 lists the symmetries of the stability eigenvectors of equilibria E_1 to E_3 .

²³ In addition to the equilibria, the KS system has pairs of relative equilibria (2.16) with fixed profiles moving at constant speed $\pm c$, that is, $u(x - ct, t)$, so they travel to the right for $c > 0$.

$$u(x \pm ct, t) = u(x, 0) \cdot u_q(x)$$

Drop

²²PC: don't you want to refer to the symmetry section, say that they have only $k = 2j$, $k = 3j$ Fourier components, respectively?

²³PC: Table 5: replace $D(m)$ by $\tau_{1/m}$ (?),
 $A(L/4)E_n$ symmetry by $\tau_{1/4}E_n$ (?)
link caption to equations in symmetry section

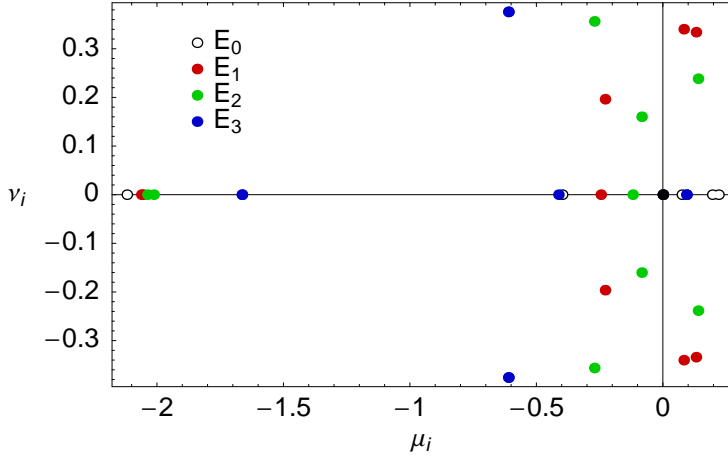


FIG. 5.2. Leading equilibrium stability eigenvalues, $L = 22$ system size.

Consistent with the bifurcation diagram of Figure 2.2, we find two relative equilibria with velocities $c = 0.73699$ and 0.34954 which we label $TW_{\pm 1}$ and $TW_{\pm 2}$, for ‘traveling waves.’ The profiles of the two relative equilibria and their time evolution with eventual decay into the chaotic attractor are shown in Figure 5.3. The leading eigenvalues of $TW_{\pm 1}$ and $TW_{\pm 2}$ are listed in Table 5; those with $\mu > -2.5$ are also plotted in Figure 5.2.²⁴

Table 5.3 lists equilibrium energy E , the local Poincaré section return time T , radially expanding Floquet multiplier Λ_e , and the least contracting Floquet multiplier Λ_c for all $L = 22$ equilibria and relative equilibria. The return time $T = 2\pi/\mu_e$ is given by the imaginary part of the leading complex eigenvalue, the expansion multiplier per one turn of the most unstable spiral-out by $\Lambda_e \approx \exp(\mu_e T)$, and the contraction rate along the slowest contracting stable eigendirection by $\Lambda_c \approx \exp(\mu_c T)$. We learn that the shortest ‘turn-over’ time is $\approx 10 - 20$, and that if there exist horseshoe sets of unstable periodic orbits associated with these equilibria, they have unstable multipliers of order of $\Lambda_e \sim 5 - 10$, and that they are surprisingly thin in the folding direction, with contracting multipliers of order of 1-4%, as in ref. [20].

5.1. Unstable manifolds of equilibria and their heteroclinic connections. In this section we explore the structure of unstable manifolds of the equilibria. As shown in Table 5, the E_1 equilibrium has two unstable planes within which the solutions are spiralling out (that is, two pairs of complex conjugate eigenvalues). The E_2 has one such plane, while the E_3 has two real positive eigenvalues, so the solutions are moving radially away from the equilibrium within the plane spanned by the corresponding eigenvectors. Since E_1 has a larger unstable subspace, it is expected to have much less influence on the long time dynamics compared to E_2 and E_3 .

To construct an invariant manifold containing solutions corresponding to the pair of unstable complex conjugate eigenvalues, $\lambda = \mu \pm i\nu$, $\mu > 0$, we start with a set of initial conditions near equilibrium E_k ,

$$a(0) = a_{E_k} + \epsilon \exp(\delta) e^{(j)}, \quad (5.1)$$

²⁴PC: dropped this: “The eigenvectors do not belong to any of the symmetric subspaces of Kuramoto-Sivashinsky equation discussed in sect. 2.1.”

TABLE 5.1

Leading eigenvalues $\lambda_j = \mu_j \pm i\nu_j$ and symmetries of the corresponding eigenvectors of KS equilibria and relative equilibria for $L = 22$ system size. We have used as our reference states the ones that lie within the antisymmetric subspace \mathbb{U}^- , and also listed the symmetries of the $L/4$ translated ones.

E_1	μ_j	ν_j	Symmetry	$\tau_{1/4}E_n$	Symmetry
$\lambda_{1,2}$	0.1308	0.3341	-	-	-
$\lambda_{3,4}$	0.0824	0.3402	R_1	-	\bar{L}
λ_5	0	-	-	-	-
$\lambda_{6,7}$	-0.2287	0.1963	R_1	u^+	\bar{L}
λ_8	-0.2455	-	-	-	-
λ_9	-2.0554	-	R_1	-	\bar{L}
λ_{10}	-2.0619	-	-	-	-
E_2					
$\lambda_{1,2}$	0.1390	0.2384	R_1	-	\bar{L}
λ_3	0	-	$\tau_{1/2}$	-	$\tau_{1/2}$
$\lambda_{4,5}$	-0.0840	0.1602	\bar{L}	-	R_1
λ_6	-0.1194	-	$\tau_{1/2}$	-	$\tau_{1/2}$
$\lambda_{7,8}$	-0.2711	0.3563	$R_1, \bar{L}, \tau_{1/2}$	-	$R_1, \bar{L}, \tau_{1/2}$
λ_9	-2.0130	-	\bar{L}	-	R_1
λ_{10}	-2.0378	-	R_1	-	\bar{L}
E_3					
λ_1	0.0933	-	R_1	-	\bar{L}
λ_2	0.0933	-	-	-	-
λ_3	0	-	$\tau_{1/3}$	-	$\tau_{1/3}$
λ_4	-0.4128	-	$R_1, \tau_{1/3}$	-	$\bar{L}, \tau_{1/3}$
$\lambda_{5,6}$	-0.6108	0.3759	R_1	-	\bar{L}
$\lambda_{7,8}$	-0.6108	0.3759	-	-	-
λ_9	-1.6641	-	-	-	-
λ_{10}	-1.6641	-	R_1	-	\bar{L}
$TW_{\pm 1}$					
$\lambda_{1,2}$	0.1156	0.8173	-	-	-
$\lambda_{3,4}$	0.0337	0.4189	-	-	-
λ_5	0	-	-	-	-
λ_6	-0.2457	-	-	-	-
$\lambda_{7,8}$	-0.3213	0.9813	-	-	-
$TW_{\pm 2}$					
λ_1	0.3370	-	-	-	-
λ_2	0	-	-	-	-
$\lambda_{3,4}$	-0.0096	0.6288	-	-	-
$\lambda_{5,6}$	-0.2619	0.5591	-	-	-
$\lambda_{7,8}$	-0.3067	0.0725	-	-	-

where δ takes the set of values uniformly distributed in the interval $[0, 2\pi\mu/\nu]$, $e^{(j)}$ is a unit vector in the unstable plane, and $\epsilon > 0$ is small.

The manifold starting within the first unstable plane of E_1 , with eigenvalues $0.1308 \pm i0.3341$, is shown in Figure 5.4. It appears to fall directly into the chaotic attractor. The behavior of the manifold starting within the second unstable plane of E_1 , eigenvalues $0.0824 \pm i0.3402$, is remarkably different: as can be seen in Figure 5.5, all orbits within the manifold converge to the equilibrium E_2 . The manifold also contains a heteroclinic connection from E_1 to E_3 , and is bordered by the λ_1 unstable manifold of E_3 .²⁵

²⁶ The two-dimensional unstable manifold of E_2 is shown in Figure 5.6. All orbits within the manifold converge to E_2 shifted by $L/4$. So this manifold can be viewed

²⁵PC: explain how this is due to symmetry, explicit reference to Kevrekidis

²⁶PC: Figure 5.7: projection base same as in the Figure 5.6 merge with Figure 5.9 into one figure.

Change
Symmetry
labels .

Because
of the
symmetries

TABLE 5.2

Experimental layout of Table 5 symmetries (incomplete, just testing the layout). Need a rational way to label symmetries. The main thing we care about is whether eigenvector is in \mathbb{U}^- , in which case its global continuation remains within \mathbb{U}^- .

	μ_j	ν_j	R	$\tau_{1/2}$
E ₂				
$\lambda_{1,2}$	0.1390	0.2384	R_1	\mathbb{U}^-
λ_3	0		$\tau_{1/2}$	$\tau_{1/2}$
$\lambda_{4,5}$	-0.0840	0.1602	\mathbb{U}^-	R_1
λ_6	-0.1194		$\tau_{1/2}$	$\tau_{1/2}$
$\lambda_{7,8}$	-0.2711	0.3563	$R_1, \mathbb{U}^-, \tau_{1/2}$	$R_1, \mathbb{U}^-, \tau_{1/2}$
λ_9	-2.0130		\mathbb{U}^-	R_1
λ_{10}	-2.0378		R_1	\mathbb{U}^-
E ₃				
λ_1	0.0933		R_1	\mathbb{U}^-
λ_2	0.0933		-	-
λ_3	0		$\tau_{1/3}$	$\tau_{1/3}$
λ_4	-0.4128		$R_1, \tau_{1/3}$	$\mathbb{U}^-, \tau_{1/3}$
$\lambda_{5,6}$	-0.6108	0.3759	R_1	\mathbb{U}^-
$\lambda_{7,8}$	-0.6108	0.3759	-	-

TABLE 5.3

Properties of equilibria and relative equilibria determining the system dynamics in their vicinity. T is characteristic time scale of the dynamics, Λ_e and Λ_c are the expansion and contraction rates.

	E	T	Λ_e	Λ_c
E ₁	0.2609	18.81	4.79	0.04
E ₂	0.4382	26.35	5.99	0.03
E ₃	1.5876	10.71	9.92	0.01
TW _{±1}	0.4649	?	?	-
TW _{±2}	0.6048	?	?	Dont need ?

as a homoclinic connection. It also contains a pair of heteroclinic connections from E₂ to E₃.

The equilibrium E₃ has a pair of real unstable eigenvalues equal to each other. Therefore, within the plane spanned by the corresponding eigenvectors, the orbits move radially away from the equilibrium. In order to trace out the unstable manifold, we start with a set of initial conditions within the unstable plane

$$a(0) = a_{E_3} + \epsilon(v_1 \cos \phi + v_2 \sin \phi), \quad \phi \in [0, 2\pi], \quad (5.2)$$

where v_1 and v_2 are orthonormal vectors within the plane spanned by the two unstable eigenvectors, seeded as in (5.1). The unstable manifold of E₃ is shown in Figure 5.8. The 3-fold symmetry of the manifold is related to the symmetry of E₃ with respect to translation by $L/3$. The manifold contains heteroclinic orbits connecting E₃ to three different points of the continuum of equilibria E₂ translated by 0 and $\pm L/6$. Note that there are two different heteroclinic orbits (B and C) connecting E₃ to the same point in the E₂ continuum. Note also that the segments of orbits B and C between E₃ and E₂ in Figures 5.5 and 5.6 represent the same heteroclinic connections as orbits B and C in Figure 5.8.

²⁷ In Figure 5.9 the equilibrium E₁ of Figure 5.9(a) is represented by the point E₁, and its unstable manifold can be examined in great detail. To each equilibrium point

¶PRIVATE

²⁷PC: if there is something useful in this paragraph, incorporate into the text, the rest of this file goes to flotsam.tx.

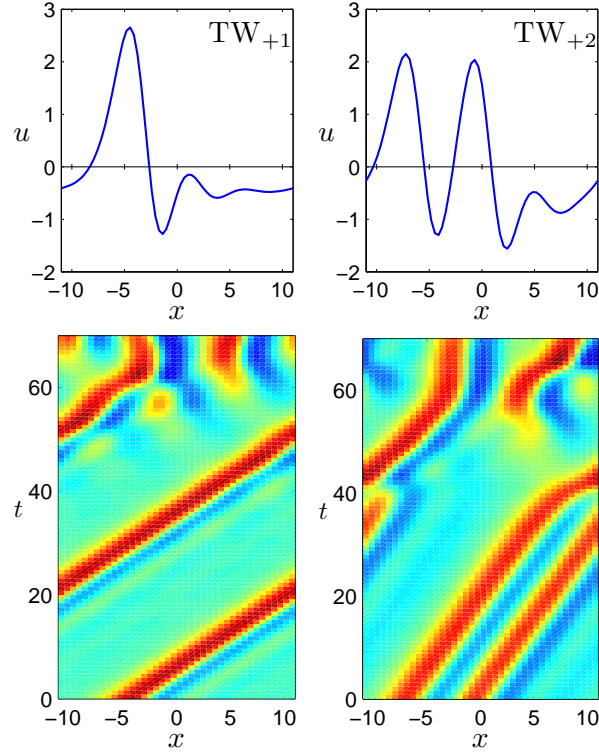


FIG. 5.3. Relative equilibria: TW_{+1} with velocity $c = 0.737$ and TW_{+2} with velocity $c = 0.350$. TW_{+2} belongs to the bifurcation branch starting at point M in Figure 2.2. The upper panels show the relative equilibria profiles. The lower panels show evolution of slightly perturbed relative equilibria and their decay into generic turbulence. Each relative equilibrium has a reflection symmetric partner related by $u(x) \rightarrow -u(-x)$ travelling with velocity $-c$.

corresponds a continuous family of equilibria, and this leads to an unexpected feature of such flows: While in dimensions higher than 2 heteroclinic connections are a rarity (likelihood that unstable manifold of one equilibrium precisely hits another equilibrium point is zero), for flows with continuous symmetries intersections of unstable manifolds with continuous families of equivalent equilibria are common. Figure 5.9 shows such heteroclinic connections. These connections partition the state space, and will be the basis of our construction of symbolic dynamics.

5.5 – 5.8

for $L=22$

offer invariant

6. Relative periodic orbits. The relative periodic orbits satisfy the condition $u(x + \ell, T) = u(x, 0)$, where T is the period and ℓ the phase shift of relative periodic orbit. We have limited our search to orbits with $T < 200$ and found over 250 prime orbits with $\ell > 0$. Each relative periodic orbit with phase shift $\ell \neq 0$ has a reflection symmetric partner $u(x) \rightarrow -u(-x)$ with phase shift $-\ell$. We have also found over 50 periodic orbits, all of which possessing the symmetry $u(x, T/2) = \mathbf{R}u(x, 0) = -u(-x, 0)$ discussed in Sect. 2.4.

type b)

The search has not been exhaustive, and there are likely to be more orbits with $T < 200$, especially with longer periods. However, the orbits we have found provide a representative sample of typical periodic and relative periodic orbits and approximate well the chaotic attractor (since they were located using seeds obtained from close

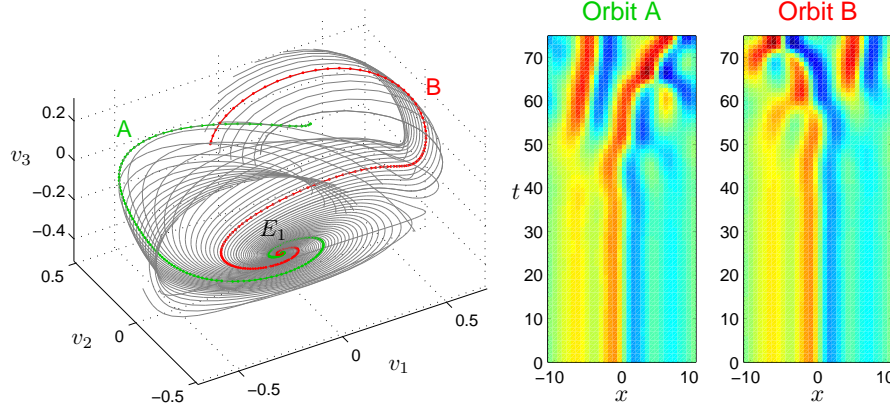


FIG. 5.4. The left panel shows the unstable manifold of equilibrium E_1 starting within the plane corresponding to the first pair of unstable eigenvalues. The coordinate axes v_1 , v_2 , and v_3 are constructed from vectors $\text{Re } \mathbf{e}^{(1)}$, $\text{Im } \mathbf{e}^{(1)}$, and $\text{Re } \mathbf{e}^{(6)}$ by Gram-Schmidt orthogonalization. The right panel shows spatial representation of two orbits A and B. The change of color from blue to red indicates increasing values of $u(x)$.

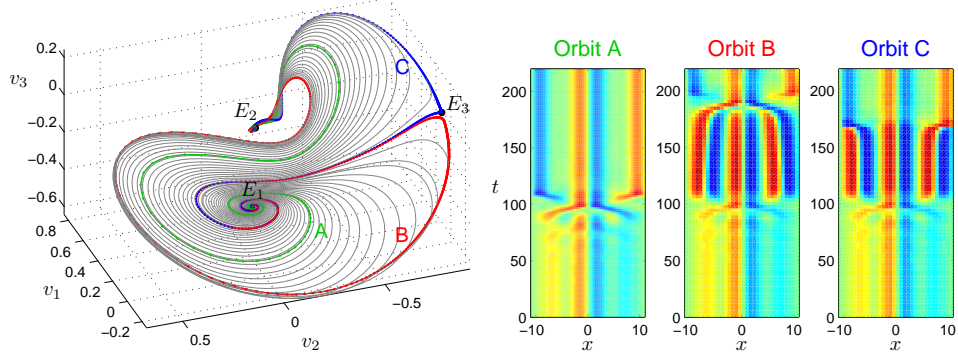


FIG. 5.5. The left panel shows the unstable manifold of equilibrium E_1 starting within the plane corresponding to the second pair of unstable eigenvalues. The coordinate axes v_1 , v_2 , and v_3 are constructed from vectors $\text{Re } \mathbf{e}^{(3)}$, $\text{Im } \mathbf{e}^{(3)}$, and $\text{Re } \mathbf{e}^{(6)}$ by Gram-Schmidt orthogonalization. The right panel shows spatial representation of three orbits. Orbits B and C pass close to the equilibrium E_3 .

returns within the chaotic dynamics).

Figure 6.1 (a) shows the relative periodic orbits in the plane (T, ℓ) . Not much is learned from such plot other than that for longer periods the relative periodic orbits are scattered over the whole (T, ℓ) .

The stability of the orbits is determined by their Lyapunov exponents, defined as

$$s_j = \mu_j/T, \quad (6.1)$$

where $\Lambda_j = e^{\mu_j \pm i\nu_j}$ are the Floquet multipliers of $J_p = g(\ell)J^T(a)$.²⁸

As could be expected from the calculation of the Lyapunov exponents of the chaotic dynamics discussed in Sect. 4, for all periodic and relative periodic orbits we

Explain
in terms
of
symmetries
refer to
Tab. 5.1

²⁸PC: do not like notation s_j for ‘Lyapunov exponent’ but let it be, for now...

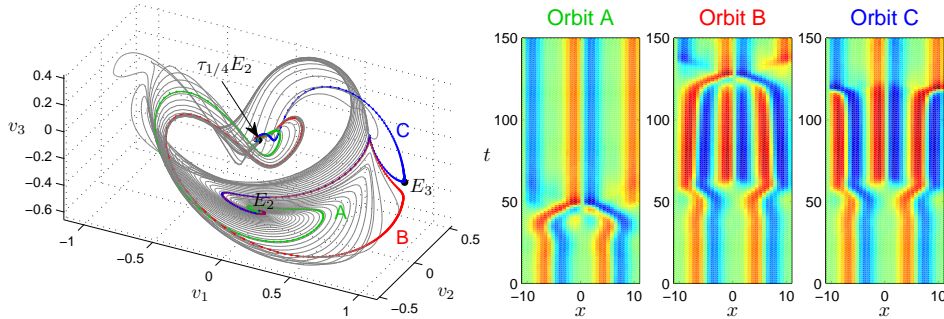


FIG. 5.6. The left panel shows the two-dimensional unstable manifold of equilibrium E_2 . The coordinate axes v_1 , v_2 , and v_3 are constructed from vectors $\text{Re } \mathbf{e}^{(1)}$, $\text{Im } \mathbf{e}^{(1)}$, and $\mathbf{e}^{(7)}$ by Gram-Schmidt orthogonalization. The right panel shows spatial representation of three orbits. Orbits B and C pass close to the equilibrium E_3 . See Figure 5.7 for a different visualization.

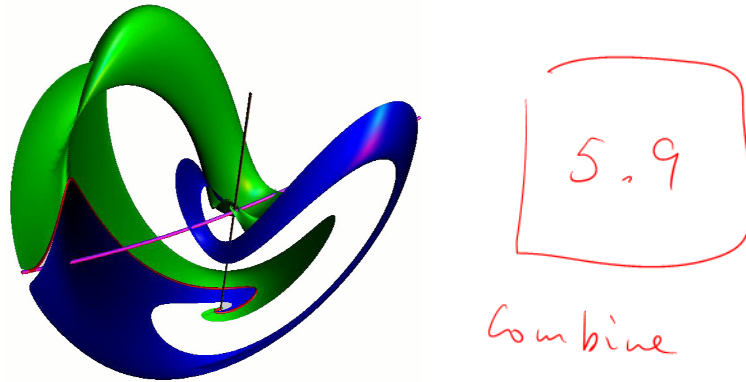


FIG. 5.7. (blue/green) The unstable manifold of E_2 equilibrium. (black line) The circle of E_2 equilibria related by the translation invariance. (purple line) The circle of E_3 equilibria. (red) The heteroclinic connection from the E_2 equilibrium to the E_3 equilibrium splits the manifold into two parts, colored (blue) and (green). See Figure 5.6 for a different visualization.

have found, only four Lyapunov exponents are dynamically relevant, with the remaining ones being very negative, indicating strong contraction towards the 4-dimensional manifold containing the chaotic attractor. Out of the four relevant exponents, two are equal to zero, corresponding to time and space translational invariance of the orbits. Of the remaining two, one is always positive, while the second one is either positive or negative, indicating non-hyperbolicity of the chaotic attractor through unstable dimension variability [17].

The scatter of the largest Lyapunov exponents of periodic and relative periodic orbits is shown in Figure 6.1 (b). In this case a tendency of accumulation toward the largest Lyapunov exponent 0.048 of the chaotic attractor can be noted. This, however, is in part an artifact of initializing the relative periodic orbit searches by near recurrences in long-time state space trajectories.

Next we describe several types of relative periodic orbits.

6.1. Short relative periodic orbits. The small period relative periodic orbits outline the coarse structure of the chaotic attractor, while the longer period relative periodic orbits resolve the finer details of the dynamics without significant modifica-

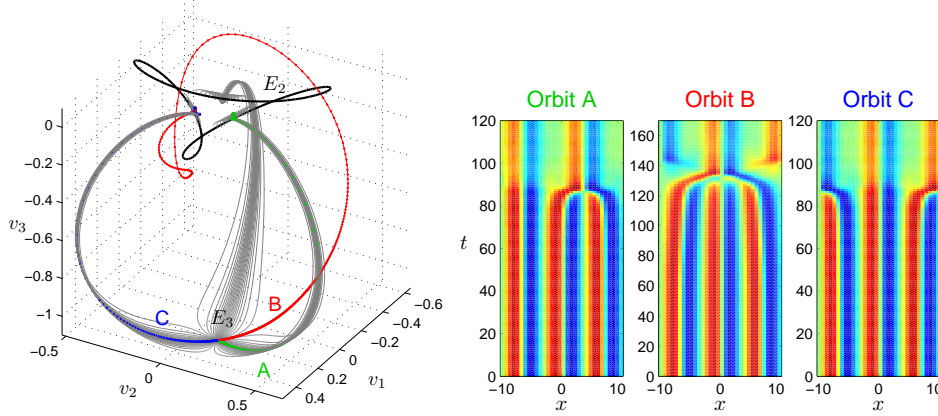


FIG. 5.8. The left panel shows the two-dimensional unstable manifold of equilibrium E_3 . The coordinate axes v_1 , v_2 , and v_3 are constructed from vectors $e^{(1)}$, $e^{(2)}$, and $e^{(4)}$ by Gram-Schmidt orthogonalization. The black line shows a family of E_2 equilibria related by translational symmetry. The right panel shows spatial representation of three orbits. Orbits B and C are two different heteroclinic orbits connecting E_3 to the same point on the E_2 line.

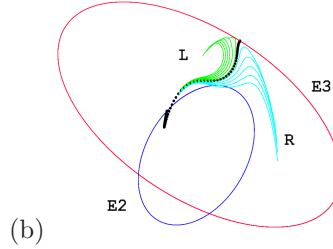


FIG. 5.9. (b) E_2 equilibrium to E_3 equilibrium heteroclinic connection. Here we omit the unstable manifold of E_2 , keeping only a few neighboring trajectories in order to indicate the unstable manifold of E_3 . The E_2 and E_3 families of equilibria arising from the continuous translational symmetry of KS on a periodic domain are indicated by the two circles. *Edit the cage of heteroclinic connections, xfig file rpo_ks/figs/ks22_E1_UM_diag.fig and rpo_ks/figs/ks22_E2_UM_diag.fig*

tion of this structure.

The first five orbits with the shortest period we have found are shown in Figure 6.2. The shortest orbit with $T = 16.4$ is also the most unstable, with one positive Lyapunov exponent equal 0.328. The other short orbits are less unstable, with the largest Lyapunov exponent, s_1 , in the range 0.018 – 0.073.
29

We have found relative periodic orbits which stay close to the unstable manifold of E_2 . As is illustrated in Figure 6.3, all such orbits have shift $\ell \approx L/4$, similar to the shift of orbits within the unstable manifold of E_2 , which start at E_2 and converge to $\tau_{L/4}E_2$ (see Figure 5.6). This confirms that the ‘cage’ of unstable manifolds of equilibria plays an important role in organizing the chaotic dynamics of the Kuramoto-Sivashinsky equation.

²⁹RLD: I've split the Figure 6.2 plots and put them in the tabular, but I don't know how to place label t to the left of the figures. Please fix this if you know how. Otherwise I can include t in the leftmost figure, but it will be a bit tricky since the aspect ratio of this figure will be different from the others.

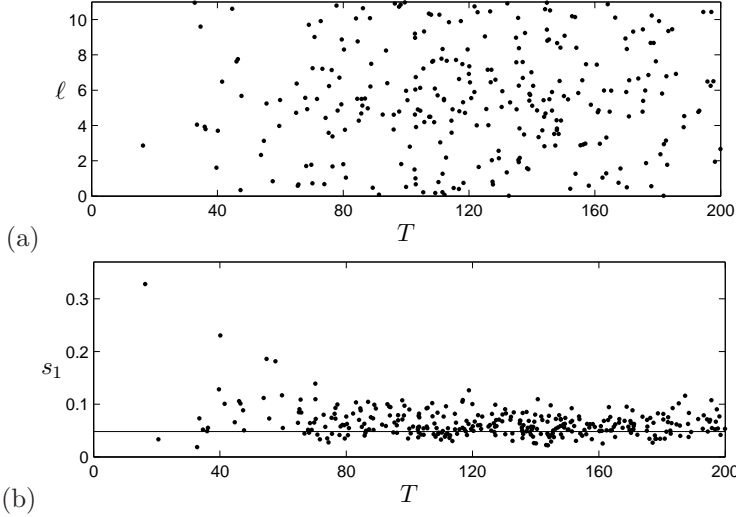


FIG. 6.1. (a) Relative periodic orbits of Kuramoto-Sivashinsky equation with period T and shift $\ell > 0$. (b) The largest Lyapunov exponents 6.1 of all periodic orbits and relative periodic orbits. The horizontal line indicates the value 0.048 of the largest Lyapunov exponent of the chaotic attractor.

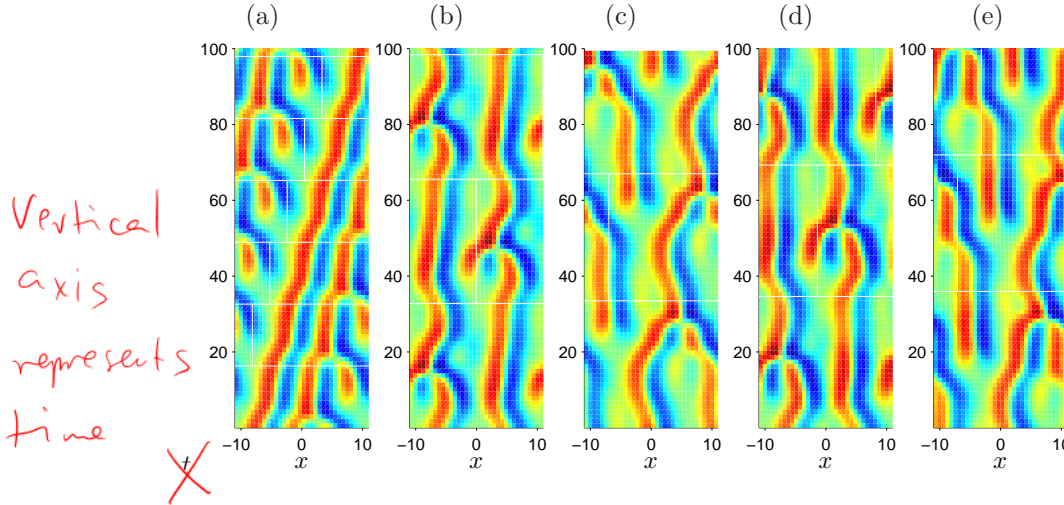


FIG. 6.2. Short period relative periodic orbits of Kuramoto-Sivashinsky equation with $L = 22$: (a) $T = 16.3$, $\ell = 2.86$; (b) $T = 32.8$, $\ell = 10.96$; (c) $T = 33.5$, $\ell = 4.04$; (d) $T = 34.6$, $\ell = 9.60$; (e) $T = 36.0$, $\ell = 3.93$. Horizontal and vertical white lines indicate periodicity and phase shift of the orbits, respectively.

6.2 Periodic Orbits. As discussed in Sect. 2.4, a relative periodic orbit will be periodic, that is, $\ell = 0$, if it either (a) lives within the \mathbb{U}^- antisymmetric subspace $-u(-x, 0) = u(x, 0)$, or (b) returns to its reflection after half-period: $u(x, T/2) = -u(-x, 0)$. The dynamics of Kuramoto-Sivashinsky equation in the antisymmetric subspace and periodic orbits with symmetry (a) have been investigated previously [3, 19, 20]. The KS equation with $L = 22$ does not have any periodic orbits of this type.

All the periodic orbits we have found so far have symmetry (b). Some of the shortest periodic orbits we have found are shown in Figure 6.4. Several periodic

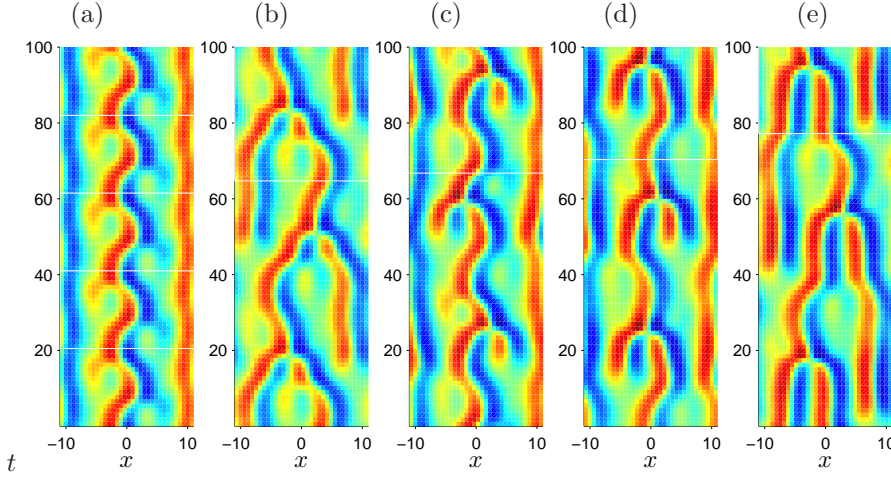


FIG. 6.4. Periodic orbits of Kuramoto-Sivashinsky equation with $L = 22$: (a) $T = 20.5$; (b) $T = 64.7$; (c) $T = 66.8$; (d) $T = 70.3$; (e) $T = 77.2$.

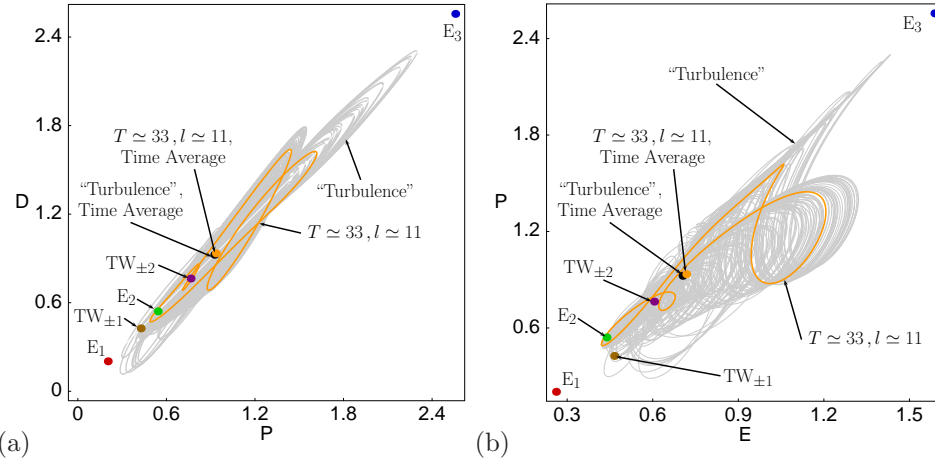


FIG. 6.5. (a) Power input P vs. dissipation rate D (b) energy E vs. dissipation rate D , for several equilibria and relative equilibria, a relative periodic orbit, and a typical ‘turbulent’ long-time trajectory. System size $L = 22$.

is different from low-dimensional chaos, insofar that the determination of one magic periodic orbit could yield all long-time predictions. Regrettably, not true - as always, here too one needs a hierarchy of periodic orbits of increasing length to obtain accurate predictions [4].

The most one can say is that if points are clearly separated in an (E, P, D) plot (for example, in Figure 6.2 E_1 equilibrium is not part of the recurrent set), they are also separated in the full state space. Converse is not true - states of very different topology can have similar energies.

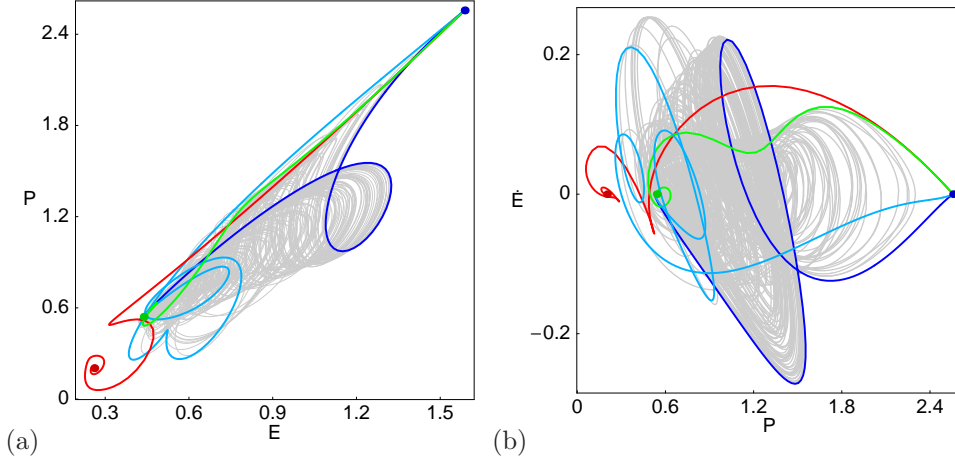


FIG. 6.6. Two projections of the (E, P, \dot{E}) representation of the flow. E_1 (red), E_2 (green), E_3 (blue), connections from E_2 to E_3 (green), from E_1 to E_3 (red) and from E_3 to E_2 (shades of blue), superimposed over a generic long-time ‘turbulent’ trajectory (grey). System size $L = 22$.

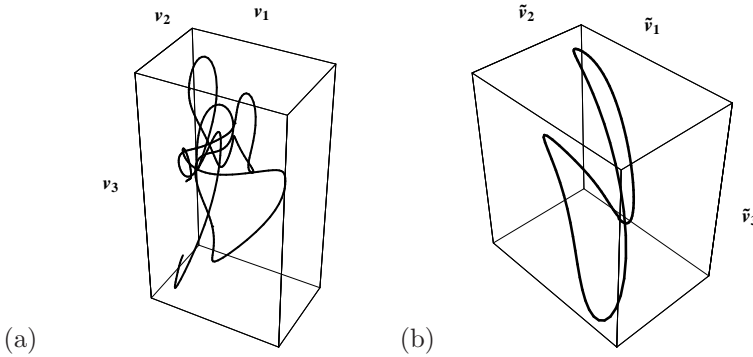


FIG. 6.7. The which appears well embedded within the turbulent flow. relative periodic orbit with $(T_p, \ell_p) = (33.5, 4.04)$ from Figure 6.2(c) in: (a) State space, traced for four periods T_p . The coordinate axes v_1 , v_2 , and v_3 are those of Figure 5.6. (b) Mean velocity frame.

Least unstable relative periodic orbits ???.³² Out of 30 relative periodic orbits we find, only three are periodic. The orbit with $T_p = 95.25$ has a very small *Drop* $d = -6.5 \times 10^{-7}$, but it is not periodic (we checked this by decreasing the integration step size and increasing the number of modes).

Sets of relative periodic orbits are difficult to visualize simultaneously.

~~options.~~

Somewhat better visualization is in the *mean velocity frame*, that is, a reference frame that rotates with velocity $v_p = \ell_p/T_p$. In the mean velocity frame a relative periodic orbit becomes a periodic orbit, see for example (6.3).³³ Mean velocity frame

Figure 6.7

³²ES: The names of the relative periodic orbit figure files follow the convention `rpoL-T-d.epss`, with suffixes `cm` and `u` indicating mean velocity frame and `u` representation respectively.

³³PC: I ordered a new laptop so I can open this mega.pdf, but until that time, I can only look separately at the individual figures in Figure 6.3. They seem to illustrate the idea nicely. Re. Figure 6.3: Why not take the relative periodic orbit $(T_p, \ell_p) = (32.8, 10.96)$ from Figure 6.2(c). BTW, are you sure that this is not $(T_p, \ell_p) = (32.8, 11)$? It is suspiciously close to $2T_p$ periodic orbit.

visualization helps quite a bit. Put a black (green, respectively) dot twice thickness of the line every time unit; it will enable you to see where the motion is slow and where it is fast. Mark the initial point on both mean velocity relative periodic orbit and on equilibrium in mean velocity frame with a fat triangle indicating the direction, so we can see how they both move. Probably at the opposite ends of the two curves - mean velocity frame is the mean motion.

Each relative periodic orbit has its own mean velocity frame - and within it, equilibrium move on circles (or worse - because in higher Fourier modes they do more complicated things), and it is important to know where the equilibrium is at a given instant.

As the shift d is defined mod L , better to state for each relative periodic orbit its mean velocity $c_p = \ell_p/T_p$, where ℓ_p is measured on the line (not on the circle). c_p is preferable to angle $2\pi\ell_p/L$ as it does not vary in $L \rightarrow \text{large limit}$ (just like $\sqrt{2}$ wavelength estimate is independent of system size).

Another convenient way to plot equilibria and relative equilibria on a periodic domain L is to plot u_x vs. u as a curve parametrized by $x \in [0, L]$. In this representation both equilibria and relative equilibria curves are stationary, but the relative equilibria points move as functions of time.

Periodic orbits and relative periodic orbits can be plotted this way, as well $u_x(x, t)$ vs. $u(x, t)$. Periodic orbits and relative periodic orbits in this representation are time-dependent ‘tubes,’ and distances between their instantaneous profiles possible could serve to define ‘nearby’ orbits for flows with continuous symmetries.

7. Summary. We have presented a detailed investigation of the topology of the Kuramoto-Sivashinsky state space for $L = 22$ system size. At first glance, turbulent dynamics visualized in the state space might appear hopelessly complex, but under a detailed examination it is much less so than feared: it is pieced together from low dimensional local unstable manifolds connected by fast transient interludes. Kuramoto-Sivashinsky and plane Couette flow equilibrium, relative equilibrium, periodic orbits and relative periodic orbits embody Hopf’s vision: repertoire of recurrent spatio-temporal patterns explored by turbulent dynamics. We used the equilibria, relative equilibria and relative periodic orbits as a probe to explore the state space topology and chaotic dynamics. Equilibria are important because they set up a coarse description of typical state space motions.

While in general for \tilde{L} sufficiently large one expects many coexisting attractors in the state space [14], in numerical studies most random initial conditions converge to the same chaotic attractor.

The key new feature of the full, periodic domain KS is its continuous translational symmetry, with attendant continuous families of relative equilibria (traveling waves) and relative periodic orbits. Relative periodic orbits, in particular, require rethinking dynamical systems approach to constructing symbolic dynamics.

At present the theory is in practice applicable only to systems with a low intrinsic dimension. If the system is very turbulent (a description of its long time dynamics requires a space of high intrinsic dimension) we are out of luck.

In a long run, the hope is that the periodic orbit theory can be applied to real-world problems, such as moderately turbulent Navier-Stokes flows, and use calculated

ES: Because the shift 10.96 is so close to $L/2$, the trajectory in state space looks like almost retracing itself so the idea of simplification was not illustrated. The numerics are good far beyond the second decimal figure and there is no reason not to expect rpo’s with shift close to $L/2$, so I am not in doubt it is an rpo.

Rigid geometry of ph. space in term of equilibria

Outstanding : Symb. dyn.
What happens when $L \rightarrow \infty$

results to match or predict experimental data, or to check and modify the assumptions underlying specific turbulence models.

³⁴

Acknowledgments. We are grateful to Y. Lan for pointing out to us the existence of the E_1 equilibrium at the $L = 22$ system size.

Appendix A. Solving Kuramoto-Sivashinsky equation numerically.

The Kuramoto-Sivashinsky equation in terms of Fourier modes:

$$\hat{u}_k = \mathcal{F}[u]_k = \frac{1}{L} \int_0^L u(x, t) e^{-ikx/\tilde{L}} dx, \quad u(x, t) = \mathcal{F}^{-1}[\hat{u}] = \sum_{k \in \mathbb{Z}} \hat{u}_k e^{ikx/\tilde{L}} \quad (\text{A.1})$$

is given by

$$\dot{\hat{u}}_k = [(k/\tilde{L})^2 - (k/\tilde{L})^4] \hat{u}_k - \frac{ik}{2\tilde{L}} \mathcal{F}[(\mathcal{F}^{-1}[\hat{u}])^2]_k. \quad (\text{A.2})$$

Since u is real, the Fourier modes are related by $\hat{u}_{-k} = \hat{u}_k^*$.

The above system is truncated as follows: The Fourier transform \mathcal{F} is replaced by its discrete equivalent

$$a_k = \mathcal{F}_N[u]_k = \sum_{n=0}^{N-1} u(x_n) e^{-ikx_n/\tilde{L}}, \quad u(x_n) = \mathcal{F}_N^{-1}[a]_n = \frac{1}{N} \sum_{k=0}^{N-1} a_k e^{ikx_n/\tilde{L}}, \quad (\text{A.3})$$

where $x_n = 2\pi\tilde{L}/N$ and $a_{N-k} = a_k^*$. Since $a_0 = 0$ due to galilean invariance and setting $a_{N/2} = 0$ (assuming N is even), the number of independent variables in the truncated system is $N - 2$. The truncated system looks as follows:

$$\dot{a}_k = v_k(a) = [(k/\tilde{L})^2 - (k/\tilde{L})^4] a_k - \frac{ik}{2\tilde{L}} \mathcal{F}_N[(\mathcal{F}_N^{-1}[a])^2]_k. \quad (\text{A.4})$$

where $k = 1, \dots, N/2 - 1$. Note that, since $a_k \in \mathbb{C}$, (A.4) represents a system of $N/2 - 1$ coupled ordinary differential equations. The discrete Fourier transform \mathcal{F}_N can be computed by FFT. In Fortran and C, the routine **REALFT** from Numerical Recipes can be used.

In order to find the Jacobian of the solution, or compute Lyapunov exponents of the Kuramoto-Sivashinsky equation, one needs to solve the equation for a displacement vector b in the tangent space:

$$\dot{b} = \frac{\partial v(a)}{\partial a} b. \quad (\text{A.5})$$

Since \mathcal{F}_N is a linear operator, it is easy to show that

$$\dot{b}_k = [(k/\tilde{L})^2 - (k/\tilde{L})^4] b_k - \frac{ik}{\tilde{L}} \mathcal{F}_N[\mathcal{F}_N^{-1}[a] \cdot \mathcal{F}_N^{-1}[b]], \quad (\text{A.6})$$

where the dot indicates componentwise product of two vectors, that is, $a \cdot b = \text{diag}(a)b = \text{diag}(b)a$. This equation needs to be solved simultaneously with (A.4).

When evaluating the Jacobian of the KS flow map, $J(a, t) = \partial f^t(a)/\partial a$, the partial derivatives need to be evaluated separately with respect to the real and imaginary

³⁴PC: The real motivation for all this is that if we understand equilibria as $L \rightarrow \infty$ we might have an entry into $L = \infty$ periodic orbit theory of KS.

parts of the components of complex-valued vector a . Therefore, the initial conditions for (A.6) that yield the partial derivative of $f^t(a)$ with respect to $\text{Re } a_k$ and $\text{Im } a_k$, are $b_j(0) = 1 + 0i$ and $b_j(0) = 0 + 1i$, respectively, for $j = k$ and $b_j(0) = 0$ otherwise.
³⁵

Appendix B. Finding relative periodic orbits.

To find periodic and relative periodic orbits of the Kuramoto-Sivashinsky equation, we use multiple shooting and the Levenberg–Marquardt algorithm implemented in `lmdes` from the MINPACK software package or function `fsolve` in Matlab.

Note that the LM algorithm is able to solve underdetermined systems of equations. Therefore, there is no need to augment the system with additional equations. For example, since Lopez *et al.* used `lmdes` to find relative periodic orbits in CGLE, they did not need to augment their system with three additional equations. In fact, we have found that, with additional equations, the solver takes many more steps to converge from the same seed, or fails to converge at all. Even though both `lmdes` and `fsolve` solvers require that the number of variables does not exceed the number of equations, the additional equations can be set identically to zero.³⁶

We need to solve the system of $N - 2$ equations

$$\mathbf{g}(\ell)f^T(a) - a = 0, \quad (\text{B.1})$$

with N unknowns (a, T, ℓ) , where f^t is the flow map of the Kuramoto-Sivashinsky equation, i.e. $f^t(a) = a(t)$ is the solution of $\dot{a} = v(a)$ with initial condition $a(0) = a$.

We have tried two different implementations of the multiple shooting. The emphasis was on the simplicity of the implementations, so, even though both implementations worked equally well, each of them had its own minor drawbacks. It is not difficult to design more sophisticated implementations where these drawbacks would be eliminated.

In the first implementation, we fix the total number of steps within each shooting stage and change the numerical integrator step size h in order to adjust the total integration time to a desired value T .

Let (a_0, T_0, ℓ_0) be the starting guess for a relative periodic orbit obtained through a close return within a chaotic attractor. We require that the initial step does not exceed h_0 , so we set the number of integration steps to $n = \lceil T_0/h_0 \rceil$.

The integration step size is equal to $h = T/n$. With the number of shooting stages equal to m , the system in (B.1) is rewritten as follows

$$\begin{aligned} F^{(1)} &= f^\tau(a^{(1)}) - a^{(2)} = 0, \\ F^{(2)} &= f^\tau(a^{(2)}) - a^{(3)} = 0, \\ &\dots \\ F^{(m-1)} &= f^\tau(a^{(m-1)}) - a^{(m)} = 0, \\ F^{(m)} &= \mathbf{g}(\ell)f^{\tau'}(a^{(m)}) - a^{(1)} = 0, \end{aligned} \quad (\text{B.2})$$

where $\tau = \lfloor n/m \rfloor h$, $\tau' = nh - (m-1)\tau$, and $a^{(j)} = f^{(j-1)\tau}(a)$, $j = 1, \dots, m$.

With the Jacobian of this system given by

$$J = \begin{pmatrix} \frac{\partial F^{(j)}}{\partial a^{(k)}} & \frac{\partial F^{(j)}}{\partial T} & \frac{\partial F^{(j)}}{\partial \ell} \end{pmatrix}, \quad j, k = 1, \dots, m, \quad (\text{B.3})$$

³⁵RLD: My sincere appreciation to anybody who can word this better. PC: appreciation gratefully appreciated

³⁶RLD: This trick was discovered by my PhD student Jonathan Crofts on 30 April 2007.

the partial derivatives with respect to $a^{(k)}$ can be calculated using the solution of (A.6). The partial derivatives with respect to T are given by

$$\frac{\partial F^{(j)}}{\partial T} = \begin{cases} \frac{\partial f^\tau(a^{(j)})}{\partial \tau} \frac{\partial \tau}{\partial T} = v(f^\tau(a^{(j)}))[\lfloor n/m \rfloor]/n, & j = 1, \dots, m-1 \\ \mathbf{g}(\ell)v(f^{\tau'}(a^{(j)}))(1 - \frac{m-1}{n}\lfloor n/m \rfloor), & j = m. \end{cases} \quad (\text{B.4})$$

Note that, even though $\partial f^t(a)/\partial t = v(f^t(a))$, it should not be evaluated using equation for the vector field. The reason is that, since the flow f^t is approximated by a numerical solution, the derivative of the numerical solution with respect to the step size h may differ from the vector field v , especially for larger step sizes. We evaluate the derivative by a forward difference using numerical integration with step sizes h and $h + \delta$:

$$\frac{\partial f^{jh}(a)}{\partial t} = \frac{1}{j\delta} [f^{j(h+\delta)}(a) - f^{jh}(a)], \quad j \in \mathbb{Z}^+ \quad (\text{B.5})$$

with $t = jh$ and $\delta = 10^{-7}$ for double precision calculations. Partial derivatives $\partial F^{(j)}/\partial d$ are all equal to zero except for $j = m$, where it is given by

$$\frac{\partial F^{(m)}}{\partial d} = \frac{d\mathbf{g}}{d\ell} f^{\tau'}(a^{(m)}). \quad (\text{B.6})$$

This Jacobian is supplied to the routine `lmder` or `fsolve` augmented with two rows of zeros corresponding to the two identical zeros augmenting (B.3) in order to make the number of equations formally equal to the number of variables, as discussed above.³⁷

In the second implementation, we keep h and τ fixed and vary only $\tau' = T - (m-1)\tau$. In this case, we need to be able to determine the numerical solution of Kuramoto-Sivashinsky equation not only at times $t_j = jh$, $j = 1, 2, \dots$, but at any intermediate time as well. We do this by a cubic polynomial interpolation through points $f^{t_j}(a)$ and $f^{t_{j+1}}(a)$ with slopes $v(f^{t_j}(a))$ and $v(f^{t_{j+1}}(a))$. The difference from the first implementation is in that partial derivatives $\partial F^{(j)}/\partial T$ are zero for all $j = 1, \dots, m-1$, except for

$$\frac{\partial F^{(m)}}{\partial T} = \mathbf{g}(\ell)v(f^{\tau'}(a^{(m)})). \quad (\text{B.7})$$

which, for consistency, needs to be evaluated from the cubic polynomial, not from the flow equation evaluated at $f^{\tau'}(a^{(m)})$.³⁸

We found the second implementation more convenient.

For detecting periodic and relative periodic orbits of the Kuramoto-Sivashinsky equation with $L = 22$, we used $N = 32$, $h = 0.25$ (or $h_0 = 0.25$ within the first implementation), and the number of shooting stages such that $\tau \approx 6.0$. Once an relative periodic orbit is found, its existence in the Kuramoto-Sivashinsky PDE is verified and numerical approximation improved by increasing the number of Fourier modes ($N = 64$) and reducing the step size ($h = 0.1$).

³⁷RLD: The drawback of this scheme is that the Kuramoto-Sivashinsky equation is integrated with different step sizes, so different relative periodic orbits cannot be readily compared, since they have been approximated using different step sizes.

³⁸RLD: The drawback of this implementation is that the numerical solution of the flow is only once differentiable, so the solvers `lmder` and `fsolve` tend to sometimes slow the convergence down when the number of steps for integrating to τ' changes. But the effect is rather marginal.

B.1. Newton method for relative periodic orbit searches. The relative periodic condition is

$$u(x + \ell, t + T) = u(x, t),$$

or, in Fourier space

$$a_p = \mathbf{g}(\ell_p) f^{T_p}(a_p), \quad (\text{B.8})$$

with period T_p and shift ℓ_p . The Fourier transformation diagonalizes the rotation operator,

$$\mathbf{g}(\ell) a(t + T) = a(t), \quad \mathbf{g}_{jk}(d) = \delta_{jk} e^{ik \ell / \tilde{L}}, \quad (\text{B.9})$$

so in the Fourier representation the relative periodic condition

$$e^{ik \ell / \tilde{L}} a_k(t + T) = a_k(t) \quad (\text{no summation on } k) \quad (\text{B.10})$$

amounts to the k th mode complex plane rotation by an angle $-k d / \tilde{L}$.

Let a , T and ℓ be our guess cycle point, period, and shift, respectively. Taylor expand $\mathbf{g}(\ell_p) f^{T_p}(a_p)$ around the desired relative periodic orbit p to linear order in $(\delta a, \delta T, \delta \ell) = (a - a_p, T - T_p, \ell - \ell_p)$:

$$\left(1 - J^{(T, \ell)}\right) \delta a - \mathbf{g}(\ell) v(f^T(a)) \delta T - \mathbf{L}(\mathbf{g}(\ell) f^T(a)) \delta \ell \simeq \mathbf{g}(\ell) f^T(a) - a, \quad (\text{B.11})$$

where $J_{ij}^{(T, \ell)} = \mathbf{g}(\ell) \partial a_i(T) / \partial a_j(0)$ is the relative periodic orbit fundamental matrix, and $L_{kj} = \frac{ik}{\tilde{L}} \delta_{kj}$ is the Lie algebra translation generator.³⁹ The matrix $J^{(T, \ell)}$ has two unit eigenvalues on the relative periodic orbit p , one associated with the invariance along the direction of the flow and the other with the translational invariance of the system. Thus (B.11) needs to be augmented by two conditions to eliminate the (close to) zero eigenvalues of $\mathbf{1} - J^{(T, \ell)}$. Following ref. [26] we impose locally transverse sections conditions

$$v(a) \cdot \delta a = 0 \quad (\text{B.12})$$

$$\mathbf{L}(\mathbf{g}a) \cdot \delta a = 0. \quad (\text{B.13})$$

The requirement imposed by (B.12–B.13) on the variations of the initial δa of (B.11) is that they vanish along the directions of the flow and of infinitesimal translations.

Equations (B.11) and (B.12–B.13) can be stated compactly as a $[N+2] \times [N+2]$ matrix condition:

$$\begin{pmatrix} 1 - J^{(T, \ell)} & -\mathbf{g}(d)v(f^T(a)) & -\mathbf{L}(\mathbf{g}(\ell)f^T(a)) \\ v(a)^\dagger & 0 & 0 \\ (\mathbf{L}ga)^\dagger & 0 & 0 \end{pmatrix} \begin{pmatrix} \delta a \\ \delta T \\ \delta \ell \end{pmatrix} = \begin{pmatrix} \mathbf{g}(d)f^T(a) - a \\ 0 \\ 0 \end{pmatrix}. \quad (\text{B.14})$$

where v^\dagger denotes the adjoint of v .⁴⁰

REFERENCES

³⁹PC: recheck - factor i might be wrong

⁴⁰PC: Ruslan, explain you do not use Newton at all

- [1] JARED C. BRONSKI AND THOMAS N. GAMBILL, *Uncertainty estimates and L_2 bounds for the kuramoto-sivashinsky equation*, 2006.
- [2] A. CHENCINER. www.imcce.fr/Equipes/ASD/person/chenciner/chenciner.html.
- [3] F. CHRISTIANSEN, P. CVITANOVIC, AND V. PUTKARADZE, *Spatiotemporal chaos in terms of unstable recurrent patterns*, Nonlinearity, 10 (1997), p. 55.
- [4] P. CVITANOVIC, R. ARTUSO, R. MAINIERI, G. TANNER, AND G. VATTAY, *Chaos: Classical and Quantum*, Niels Bohr Institute, Copenhagen, 2005. ChaosBook.org.
- [5] P. CVITANOVIC AND B. ECKHARDT, *Symmetry decomposition of chaotic dynamics*, Nonlinearity, 6 (1993), p. 277. chao-dyn/9303016.
- [6] C. FOIAS, B. NICOLAENKO, G.R. SELL, AND R. TEMAM, *Inertial manifold for the Kuramoto-Sivashinsky equation*, C. R. Acad. Sci. I-Math, 301 (1985), pp. 285–288.
- [7] U. FRISCH, Z. S. SHE, AND O. THUAL, *Viscoelastic behavior of cellular solutions to the Kuramoto-Sivashinsky model*, J. Fluid Mech., 168 (1986), pp. 221–240.
- [8] LORENZO GIACOMELLI AND FELIX OTTO, *New bounds for the kuramoto-sivashinsky equation*, Comm. Pure Appl. Math., 58 (2005), pp. 297–318.
- [9] J. F. GIBSON, J. HALCROW, P. CVITANOVIC, AND F. WALEFFE, *On the geometry of state space of a turbulent plane Couette flow: I Exact coherent solutions*. In preparation, 2007.
- [10] J. M. GREENE AND J. S. KIM, *The steady states of the Kuramoto-Sivashinsky equation*, Physica D, 33 (1988), pp. 99–120.
- [11] B. HOF, C. W.H. VAN DOORNE, J. WESTERWEEL, F. T.M. NIEUWSTADT, H. FAISST, B. ECKHARDT, H. WEDIN, R. R. KERSWELL, AND F. WALEFFE, *Experimental observation of nonlinear traveling waves in turbulent pipe flow*, Science, 305 (2004), pp. 1594–1598.
- [12] P. HOLMES, J.L. LUMLEY, AND G. BERKOOZ, *Turbulence, Coherent Structures, Dynamical Systems and Symmetry*, Cambridge University Press, Cambridge, 1996.
- [13] E. HOPF, *A mathematical example displaying features of turbulence*, Comm. Appl. Math., 1 (1948), pp. 303–322.
- [14] J. M. HYMAN, B. NICOLAENKO, AND S. ZALESKI, *Order and complexity in the Kuramoto-Sivashinsky model of weakly turbulent interfaces*, Physica D, 23 (1986), pp. 265–292.
- [15] G. KAWAHARA AND S. KIDA, *Periodic motion embedded in Plane Couette turbulence: regeneration cycle and burst*, J. Fluid Mech., 449 (2001), pp. 291–300.
- [16] I. G. KEVREKIDIS, B. NICOLAENKO, AND J. C. SCOVEL, *Back in the saddle again: a computer assisted study of the Kuramoto-Sivashinsky equation*, SIAM J. Appl. Math., 50 (1990), pp. 760–790.
- [17] ERIC J. KOSTELICH, ITTAI KAN, CELSO GREBOGI, EDWARD OTT, AND JAMES A. YORKE, *Unstable dimension variability: a source of nonhyperbolicity in chaotic systems*, Phys. D, 109 (1997), pp. 81–90.
- [18] Y. KURAMOTO AND T. TSUZUKI, *Persistent propagation of concentration waves in dissipative media far from thermal equilibrium*, Progr. Theor. Phys., 55 (1976), p. 365.
- [19] Y. LAN, *Dynamical systems approach to 1-d spatiotemporal chaos – A cyclist’s view*, PhD thesis, School of Physics, Georgia Institute of Technology, Atlanta, 2004.
- [20] Y. LAN AND P. CVITANOVIC, *Unstable recurrent patterns in Kuramoto-Sivashinsky dynamics*. In preparation, 2007.
- [21] V. LÓPEZ, P. BOYLAND, M. T. HEATH, AND R. D. MOSER, *Relative periodic solutions of the Complex Ginzburg-Landau equation*, SIAM J. Appl. Dyn. Syst., 4 (2005), p. 1042.
- [22] D. MICHELSON, *Steady solutions of the Kuramoto-Sivashinsky equation*, Physica D, 19 (1986), pp. 89–111.
- [23] R. E. LA QUEY, S. M. MAHAJAN, P. H. RUTHERFORD, AND W. M. TANG, *Nonlinear saturation of the trapped-ion mode*, Phys. Rev. Lett., 34 (1974), pp. 391–394.
- [24] G. I. SIVASHINSKY, *Nonlinear analysis of hydrodynamical instability in laminar flames - I. Derivation of basic equations*, Acta Astr., 4 (1977), p. 1177.
- [25] V. SZEBEHELY, *Theory of Orbits*, Academic Press, New York, 1967.
- [26] D. VISWANATH, *Recurrent motions within plane Couette turbulence*, J. Fluid Mech., 580 (2007), pp. 339–358. arXiv:/physics/0604062.